ACS OMEGA

http://pubs.acs.org/journal/acsodf

Article

Toward Efficient Bactericidal and Dye Degradation Performance of Strontium- and Starch-Doped Fe_2O_3 Nanostructures: In Silico Molecular Docking Studies

Muhammad Ikram,* Anum Shahzadi, Ali Haider, Muhammad Imran, Shaukat Hayat, Junaid Haider, Anwar Ul-Hamid, Faiz Rasool, Walid Nabgan,* Muhammad Mustajab, Salamat Ali, and Ali Al-Shanini*

Cite This: *ACS Omega* 2023, 8, 8066−8077

Read Online

ACCESS | Metrics & More | Article Recommendations | Supporting Information

ABSTRACT: In this study, various concentrations of strontium (Sr) into a fixed amount of starch (St) and Fe_2O_3 nanostructures (NSs) were synthesized with the co-precipitation approach to evaluate the antibacterial and photocatalytic properties of the concerned NSs. The study aimed to synthesize nanorods of Fe_2O_3 with co-precipitation to enhance the bactericidal behavior with dopant-dependent Fe_2O_3. Advanced techniques were utilized to investigate the structural characteristics, morphological properties, optical absorption and emission, and elemental composition properties of synthesized samples. Measurements via X-ray diffraction confirmed the rhombohedral structure for Fe_2O_3. Fourier-transform infrared analysis explored the vibrational and rotational modes of the O−H functional group and the C═C and Fe−O functional groups. The energy band gap of the synthesized samples was observed in the range of 2.78−3.15 eV, which indicates that the blue shift in the absorption spectra of Fe_2O_3 and Sr/St-Fe_2O_3 was identified with UV−vis spectroscopy. The emission spectra were obtained through photoluminescence spectroscopy, and the elements in the materials were determined using energy-dispersive X-ray spectroscopy analysis. High-resolution transmission electron microscopy micrographs showed NSs that exhibit nanorods (NRs), and upon doping, agglomeration of NRs and nanoparticles was observed. Efficient degradations of methylene blue increased the photocatalytic activity in the implantation of Sr/St on Fe_2O_3 NRs. The antibacterial potential for *Escherichia coli* and *Staphylococcus aureus* was measured against ciprofloxacin. *E. coli* bacteria exhibit inhibition zones of 3.55 and 4.60 mm at low and high doses, respectively. *S. aureus* shows the measurement of inhibition zones for low and high doses of prepared samples at 0.47 and 2.40 mm, respectively. The prepared nanocatalyst showed remarkable antibacterial action against *E. coli* bacteria rather than *S. aureus* at high and low doses compared to ciprofloxacin. The best-docked conformation of the dihydrofolate reductase enzyme against *E. coli* for Sr/St-Fe_2O_3 showed H-bonding interactions with Ile-94, Tyr-100, Tyr-111, Trp-30, ASP-27, Thr-113, and Ala-6.

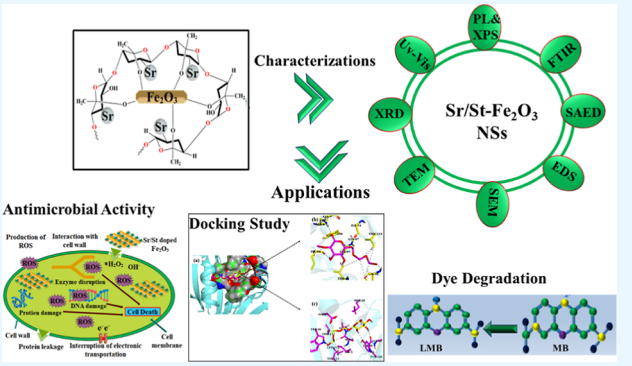

1. INTRODUCTION

A critical component of all living things is clean water. However, rapid industrialization and enormous population growth led to increased contamination of the world's water resources. The ultimatum and clean water consumption have grown significantly in agriculture. About 70, 22, and 8%, respectively, of clean water with a high pollutant range is consumed in industries, the home sector, and other forms of consumption.[1] Upon producing various goods, contaminated water from factories leaked into the shipping canal. This contaminated effluent contains several chemical components that could harm the environment. The most harmful pollutant discharged from the textile sector, agricultural resources, and urban areas is contained in chemical components. These chemical components can be either organic or synthetic dyes that damage the environment the most.[2,3] According to research, 20% of dyes produced globally were either indirectly or directly released into the environment.[4] The environment is seriously threatened by the more persistent, non-biodegradable, and aromatic molecular structures of particularly basic dyes like methylene blue (MB).[5] Many scientists and researchers have started a quest to look for multiple-level remedies to alleviate this terrible circumstance. In this context, promising technological advancements have taken place, such as bio-based contaminant utilization and development in various functionalized filtrations such as bio-filtration, ultra-

Received: December 15, 2022
Accepted: February 6, 2023
Published: February 16, 2023

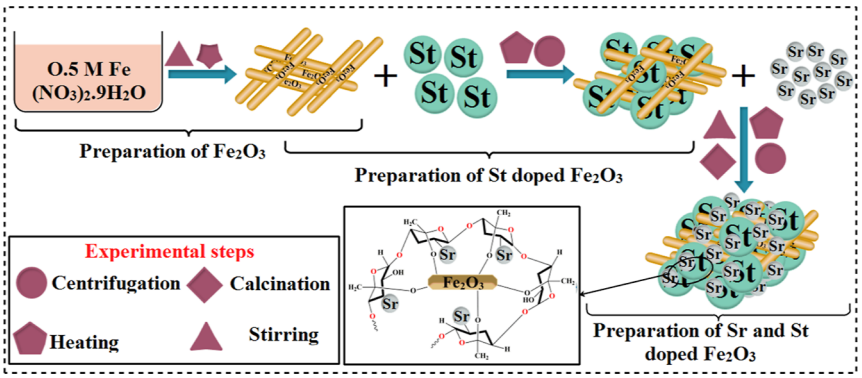

Figure 1. Schematic diagram for the structure and preparation of Sr/St-Fe_2O_3.

filtration, electro-dialysis, aerobic treatment, adsorptions,[6] and photocatalytic (PC) techniques to degrade the dyes from contaminated industrial wastewater.[7−9] Because it uses materials that contain carbon, adsorption technology is effective. In addition, it can be used as a framework to incorporate inorganic materials. The composite was created by breeding metal nanoparticles (NPs) into an organic structure and then employed for antibacterial and wastewater treatment applications.[5,10] The frontline of nanotechnology's explosive development is NPs. Hence, these constituents are superior and indispensable in many social activities owing to their distinct size-dependent properties.[11] Iron (Fe) is a recent transition metal that may be found in the crust of the Earth; it serves as the basis for modern infrastructure.[12] In comparison to other metal group components such as cobalt (Cu), nickel (Ni), gold (Au), and platinum (Pt), iron oxide has a relatively broad range of applications.[12] There are about 16 recognized iron oxides, which are created chemically when iron and oxygen interact. Rust is a type of iron(III) oxide found in nature.[13] Iron oxides are commonly and frequently used because they are cheap and essential in many biological processes. Hematite (−Fe_2O_3) is utilized frequently as catalysts,[14,15] supports,[16−18] or sensors[19,20] owing to inexpensive cost, strong corrosion resistance, and eco-friendly attributes. Additionally, Fe_2O_3 has the potential to include significant oxygen concentrations, which most likely correspond to oxygen supply through oxidation reactions. Iron oxide is a precursor for the molten iron catalyst, and it comes in three different forms: Fe_2O_3, Fe_3O_4, and FeO. Due to their inexpensive cost, high adsorption capacity, simple separation, and improved stability, iron oxide nanomaterials (NMs) are promising catalysts for industrial wastewater treatment. Iron oxide NMs are currently used in two different types of technologies for the treatment of contaminated water: (a) adsorptive/immobilization technology, which may use Fe_2O_3 NMs as a nano-sorbent type or immobilization carrier to increase removal efficiency, and (b) photocatalysts, which can use Fe_2O_3 to degrade or change toxins into a less harmful form. Nevertheless, it should now be emphasized that many technologies may use both methods.[21,22] A natural, renewable polymer derived from plants is starch (St). St is the secondary most prevalent biomass material and a renewable energy source.[23−25] St is composed in its pure form of a mixture of two polymers of an anhydroglucose unit, amylase, and amylopectin.[25] Sts are difficult to understand for many uses, including drug delivery, tissue engineering, and other biomedical ones. Excellent biological characteristics of St include biodegradability, biocompatibility, and nontoxicity.[26] Because it is renewable, biodegradable, and inexpensive, the St biopolymer may also gain interest for industrialized applications in wastewater treatment.[25] Due to their distinct physical and chemical properties, metallic NPs have attracted the most attention among all NPs in recent years. The periodic table's group II metallic elements include strontium (Sr). Sr-conjugated NPs are also effective at removing harmful pollutants from industrial wastewater and have antibacterial properties. The positive charge and capacity to absorb a small number of anionic analytes make Sr (Sr) a suitable material for water treatment.[27]

NMs have been shown to have antibacterial effects against many different types of bacteria. This includes Gram-positive *Staphylococcus aureus* (*S. aureus*) and Gram-negative *Escherichia coli* (*E. coli*). Among these, methicillin-resistant *S. aureus* (MRSA) is the most alarming because of how many people died worldwide. Approximately, 1.3 million children under the age of 5 die yearly from complications related to diarrhea caused by the bacterium *E. coli*, which is mainly spread by contaminated water. Bacterial attachment is ensured by NMs that are tiny, mobile, and conductive.[28]

In this article, we propose a low-cost synthesis of Fe_2O_3 and Sr/St-doped Fe_2O_3 (Sr/St-Fe_2O_3) with various concentrations (2 and 4%) of Sr for antimicrobial and photocatalytic activity (PCA) applications. Additionally, Sr and St dopant effects in structural, morphological, and optical properties of Fe_2O_3 are discussed. Using computational methods, scientists can probe the hidden mechanisms underlying a wide range of biological processes. The best-docked conformation of the dihydrofolate reductase (DHFR) enzyme against *E. coli* for Sr/St-Fe_2O_3 showed H-bonding interactions with Ile-94, Tyr-100, Tyr-111, Trp-30, ASP-27, Thr-113, and Ala-6, and molecular docking predictions were carried out to learn about the nanocomposites' binding propensity.

2. EXPERIMENTAL SECTION

2.1. Materials. All the chemicals and reagents, including iron(III) nitrate nonahydrate [$Fe(NO_3)_3{\cdot}9H_2O$. 98%], St ($C_6H_{10}O_5$. 97.5%), Sr(II) nitrate [$Sr(NO_3)_2$. 99.07%], sodium hydroxide (NaOH. 98.5%), and MB, were procured from Sigma-Aldrich (Germany) and Analar, respectively. The above-mentioned chemicals were of analytical grade, and all compounds were utilized with no additional purification.

2.2. Preparation of Fe_2O_3 and Sr/St-Doped Fe_2O_3 Nanostructures. Un-doped and Sr/St-doped Fe_2O_3 nanostructures (NSs) were prepared through the co-precipitation

https://doi.org/10.1021/acsomega.2c07980
ACS Omega 2023, 8, 8066−8077

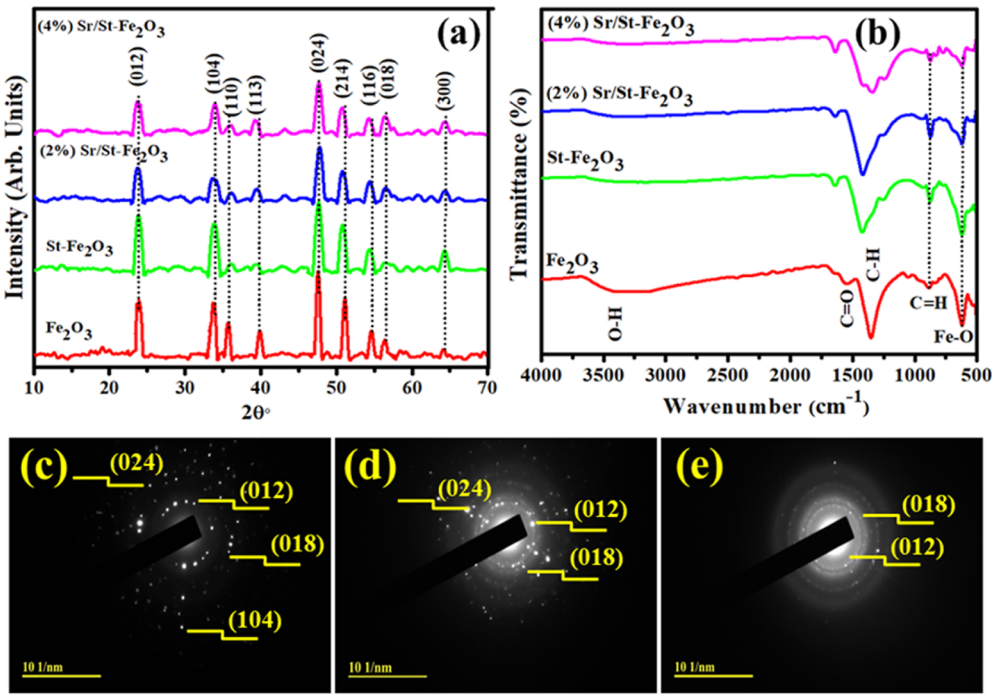

Figure 2. (a) XRD patterns of Fe_2O_3, St-Fe_2O_3, and (2, 4%) Sr/St-Fe_2O_3 NSs; (b) FTIR spectra of Fe_2O_3, St-Fe_2O_3, and (2, 4%) Sr/St-Fe_2O_3 NSs; and (c,d) SAED patterns of pristine Fe_2O_3, St-Fe_2O_3, and (4%) Sr/St-Fe_2O_3.

route, as shown in Figure 1. An appropriate amount of 0.5 M $Fe(NO_3)_2{\cdot}9H_2O$ was first dissolved in 50 mL of distilled water under vigorous stirring at 85 °C for 45 min (min). A fixed amount (0.5 g) of $C_6H_{10}O_5$ was added to the above-stirred solution. Various concentrations (2 and 4%) of Sr [using source $Sr(NO_3)_2$] were added to the St-doped Fe_2O_3 solution. The salts were precipitated at 85 °C after incorporating 0.5 M solutions of NaOH to sustain a pH value of ∼12 and finally kept at 100 °C for 1.5 h (h). The resulting precipitates were cooled, separated with centrifugation (75000 rpm, 10 min), and washed with ethanol and deionized water (DIW) to remove salts. The obtained compounds were dried by stirring at ∼400 °C for ∼4 h; the red brick-colored powders were collected after grinding to get pristine Fe_2O_3 and Sr/St-Fe_2O_3 powders.[29]

2.3. PC Activity. The current study involved the degradation of MB in the presence of Fe_2O_3, St/Fe_2O_3, and the (2, 4%) Sr/St-Fe_2O_3 NS under sunlight. The relevant samples' PCA was monitored using UV/vis spectrophotometry at room temperature. A freshly prepared solution of MB (30 mL) and synthesized samples (10 mg) were mixed before irradiation; these materials were reserved in the dark (30 min) to establish robust adsorption/desorption equilibrium between the photocatalyst and MB solution. After stirring, the combined solution was poured into a photoreactor, and a mercury (Hg) vapor lamp (400 W, 15 cm) was used as the light source. After this, 3 mL of the solution was taken out and put through a UV−vis test at different time intervals (0, 30, 60, 90, and 120 min). The λ_{max} (maximum absorption) for MB was noticed at ∼665 nm for concerned NSs. Using eq 1, the degradation (%) could be calculated[30,31]

$$\%\ \text{degradation} = \frac{C_0 - C_t}{C_t} \times 100 \quad (1)$$

where C_0 and C_t are initial and final MB concentrations, respectively.

2.4. Antimicrobial Activity. Antibacterial activity for bare Fe_2O_3, St-Fe_2O_3, and Sr/St-Fe_2O_3 with a Sr content of 2 and 4% was analyzed via the agar well diffusion method in comparison to *E. coli* (Gram-negative bacterium) and *S. aureus* (Gram-positive bacterium). The growths of both bacteria were tested on a nutrient agar medium. Utilizing a sterile cork borer, a well having a diameter of 6 mm was punched into agar plates. Petri plates were swabbed at 1.6×10^8 $CFUmL^{-1}$ (0.5 Mc-Farland standard) for *S. aureus* and *E. coli* on mannitol salt agar (MSA) and macconkey agar (MA), respectively. The swabbed Petri plates were then incubated at 37 °C for 24 h, and the inhibition zones surrounding the wells were observed. Correspondingly, the antibacterial potential was determined around the well by measuring the inhibition zone diameter (mm). Meanwhile, pristine and St-Fe_2O_3 and Sr/St-Fe_2O_3 0.5 mg/50 μL at a low and at a high 1.0 mg/50 μL concentration have been prepared in one. All wells with ciprofloxacin (CF) 5 μg/50 μL carried as the positive control, and DIW (50 μL) was used as a negative control in the comparison. Finally, the inoculation dishes were incubated aerobically at 37 °C overnight, and the inhibition zone was measured using a Vernier caliper to evaluate the bactericidal efficiency.[32,33]

2.5. Molecular Docking Analysis. DHFR converts dihydrofolate to tetrahydrofolate, is involved in the biosynthesis of purines and thymidylate, and is, hence, considered vital for the survival of bacteria.[34] In order to determine the inhibitory capability of St-Fe_2O_3 and Sr/St-Fe_2O_3, we evaluated them against DHFR from *E. coli* and *S. aureus*. The crystal structures of *E. coli*-DHFR (PDB code: 2ANQ, Resolution: 2.13)[35] were obtained from the RCSB PDB (www.rcsb.org). Similarly, DHFR from *S. aureus* has a PDB ID: 3FY8 (Resolution: 2.20).[36] To conduct the docking analysis, SYBYL-X 2.0 software was utilized. Similar to our earlier work,[37] we used SYBYL-X 2.0 to build 3-D structures of the compounds of

https://doi.org/10.1021/acsomega.2c07980
ACS Omega 2023, 8, 8066−8077

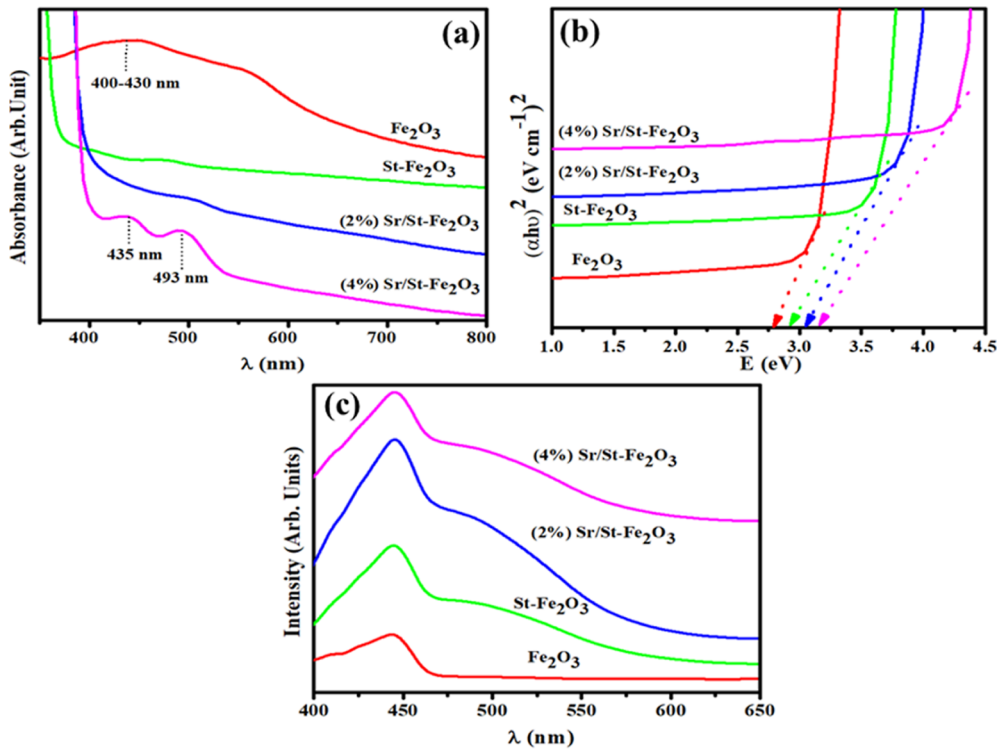

Figure 3. (a) UV−vis absorption spectra; (b) calculated energy band gap; and (c) PL emission spectra for Fe_2O_3, St-Fe_2O_3, and (2, 4%) Sr/St-Fe_2O_3 NSs.

interest and to examine NP binding interactions with the active site residues of the specified proteins.

2.6. Material Characterizations. To determine the structure of the crystal and phase of Fe_2O_3 and doped Fe_2O_3 in the 2θ range (10−70°), the Analytical XPert PRO X-ray diffraction system was employed. This system used CuKα radiation with a wavelength of 0.0154 nm. A spectroscope manufactured by PerkinElmer was utilized to determine the functional groups present in the Fourier-transform infrared (FTIR) spectra. To investigate the optical and PC measurement within the wavelength range of 350−800 nm, a UV−vis spectrophotometer, model LABDEX, was used. The morphologies and microstructures of the samples were measured by employing a JSM-6460LV field-emission scanning electron microscopy system that was linked with an energy-dispersive X-ray spectrometer. On a JASCO FP-8300 system, PL spectra were obtained for the pure and the doped Fe_2O_3. For measuring the inter-planner *d*-spacing of prepared samples, the high-resolution transmission electron microscopy (HR-TEM) equipment JEOL JEM 2100F was used.

3. RESULTS AND DISCUSSION

The prepared material's crystal structure, crystallite size, phase composition, and phase purity were analyzed through X-ray diffraction (XRD) analysis. XRD analysis was utilized for dopant-free Fe_2O_3 and Sr/St-Fe_2O_3 in the 2θ° range of 10−70° as represented in Figure 2a. Peaks were stationed at the following positions: 23.98, 33.15, 35.61, 40.21, 47.48, 52.87, 54.60, 56.22, and 64.36° that are allocated to (012), (104), (110), (113), (024), (214), (116), (018), and (300) planes of the rhombohedral structure of Fe_2O_3, respectively (JCPDS: 89-2810).[38,39] Significant variation (peak intensity increased) in St-Fe_2O_3 composite spectra was detected, which may be a confirmation of St loading into the Fe_2O_3 composite. Furthermore, peak shifting (higher angle) was noticed after 2 and 4% doping of Sr into fixed St-Fe_2O_3. The broadness in the intensities of the peaks was interpreted as good coupling of the prepared samples, which resulted in increased crystallinity and structural quality. The crystalline sizes of undoped Fe_2O_3, St-Fe_2O_3, 2% Sr/St-Fe_2O_3, and 4% Sr/St-Fe_2O_3 composites were measured as ∼48.41, ∼42.83, ∼39.51, and ∼35.72 nm, respectively, using intense peaks (012), (104), and (110) by applying the Debye−Scherrer formula.

To identify functional groups, chemical bonds in compounds, chemical structures, and hybrid molecular vibrations such as bending and stretching in a specific infrared area, the synthesized Fe_2O_3, St-Fe_2O_3, and (2, 4%) Sr/St-Fe_2O_3 were assessed in the spectral ranges of the 4000−500 cm^{-1} wavenumber as represented in Figure 2b. Furthermore, the transmittance spectrum of pristine Fe_2O_3 unveiled a functional group at ∼3437 cm^{-1} referred to as O−H stretching vibrations due to the presence of moisture in the air and C═C owing to CO_2 absorption. Furthermore, the Fe−O stretching mode has a characteristic peak at ∼621 cm^{-1},[40] which confirms the Fe_2O_3 successful formation.[40] Meanwhile, the band found at ∼883 cm^{-1} may be assigned to C═H stretching vibration.[41] The absorption peaks around 1552 and 1647 cm^{-1} correspond to symmetric and asymmetric C═O bending vibrations, respectively.[41] The small absorption peaks at ∼1784 and ∼1051 cm^{-1} were associated with C═O and C−O stretching vibrations, respectively.[42,43] In addition, the slight shifting of the peaks is associated with incorporation of St and Sr into Fe_2O_3 (Figure 2b).

A selected area electron diffraction (SAED) analysis of Fe_2O_3 and St-Fe_2O_3 and (2 and 4%) Sr/St-Fe_2O_3 NSs was performed on a small section within the sphere, as shown in Figure 2c−e. This study was conducted on a limited region within the sphere. The result shows a pattern of concentric

https://doi.org/10.1021/acsomega.2c07980
ACS Omega 2023, 8, 8066−8077

rings, suggesting that the NSs are polycrystalline in the nature of the prepared specimen. Diffraction rings inside SAED analysis were ascribed to (012), (018), (024), (104), and (110) planes which were indexed as rhombohedral structures and were found to be consistent with XRD analysis.

The absorption properties of prepared Fe_2O_3, St-Fe_2O_3, and (2, 4%) Sr/St-Fe_2O_3 NSs were examined using a UV−vis spectrometer ranging from 250 to 800 nm, as revealed in Figure 3a. Un-doped Fe_2O_3 exhibited two characteristic absorption peaks at 435 and 493 nm, corresponding to charge transfer between ligands and metals.[44] The electronic transition from the shell of 2^{d5} orbitals to Fe^{3+} ions may be the reason that Fe_2O_3 NSs exhibited absorption bands from UV to near-vis wavelengths.[45] First, magnetically coupled Fe^{3+} cations appeared in adjacent sites. Second, Fe^{3+} ligand field transition occurred and consequently transferred the charge ligand to the metal. This twofold excitation operation may be a reason for the absorption band appearing within the visible region.[46]

Furthermore, after doping with St, a clear blue shift was noted; meanwhile, upon Sr doping, similar behavior was observed. The new absorption and emission peaks (i.e., blue-shifted peak) may be the characteristic features of the formed metal−ligand complex. The binding of metal ions to the ligand caused a blue shift.[44] To calculate band gap energies (E_g) of concerned samples, the Tauc equation was used, and corresponding graphs have been plotted for $(\alpha h\nu)^2$ versus $(h\nu)$ as depicted in Figure 3b; direct E_g for Fe_2O_3 was found to be 2.78 eV which is consistent with the published literature.[46] For St-Fe_2O_3- and (2, 4%) Sr/St-doped samples, increase in E_g (2.78 to 3.15 eV) was observed, as visualized in Figure 3b. Wide-band gap semiconductors absorb high-energy wavelengths due to blue shift in the absorption edge, thus enhancing solar conversion efficiency. The reduction of a semiconductor crystal size is associated with band gap broadening. Because of this, higher absorbance of quantum energy supplied by photons with higher eV is anticipated for valence band (VB)-to-conduction band (CB) excitations and, consequently, shifting of the absorption edge.[47] The E_g of the doping concentration increased as the crystallite sizes grew; this may have been driven by diminished orientation alignment and poor crystallinity of the materials being considered.[48]

Photoluminescence (PL) spectra were used to acquire information on quantum confinement, optical properties, and energy levels of pristine and Sr/St-Fe_2O_3 samples. The quantum confinement effect is observed when the size of the particle is too small to be comparable to the wavelength of the electron. Quantum confinement effects describe electrons in terms of energy levels, potential wells, and VBs.[30] Moreover, the analyzed PL spectra for Fe_2O_3 and (2, 4 wt %) Sr/St-Fe_2O_3 materials have wavelengths between 400 and 600 nm, as demonstrated in Figure 3c. In addition, emissions could be attributed to unresolved states because pumping encourages excitations to achieve two or more than two $\bar{e}$−h+ hole pairs due to Coulomb interaction and increased photoemissions. This happens because of the interaction between Coulombs and electrons.[49]

Similarly, lower emissions resulted in a less intense band, indicating lower carrier recombination. The PL emission intensity spectrum directly correlates with the photoinduced charge carrier's (electron and holes) recombination rate. The PL spectrum with high intensity indicates a high rate recombination of electron−hole pairs, and low intensity represents high charge carrier efficiency and a low recombination rate of photoinduced charge carriers.[50] PL spectra indicate the electron−hole recombination rate that decreases the PCA. The more intense spectra for un-doped Fe_2O_3 appeared at ∼443 nm, corresponding to the blue emission. They ascribed the structural defect, such as oxygen vacancies, that frequently acts as defect donors for n-type semiconductor oxides. This would lead to new energy levels in the space between band levels.[51,52]

HRTEM micrographs predicted the morphology of the as-synthesized samples along with corresponding *d*-spacing images, as shown in Figure 4a−d. Pure Fe_2O_3 exhibits the

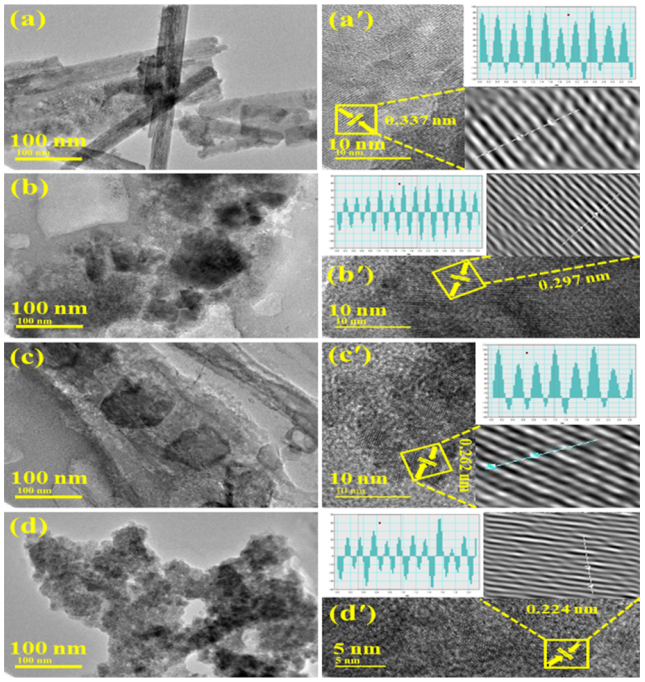

Figure 4. HR-TEM images of (a−d) Fe_2O_3, St-Fe_2O_3, and Sr/St-Fe_2O_3. (a′−d′) Interlayer *d*-spacing images with a scale bar of 100 and 10 nm.

formation of nanorods, represented in Figure 4a. The incorporation of a fixed amount of St into Fe_2O_3 showed that the agglomerated rod overlapped with St (Figure 4b). The addition of various concentrations of Sr (2 and 4%) into the binary system (starch+Fe_2O_3). showed partial interaction of nanorods and NPs. Furthermore, high order of agglomeration was observed upon doping of Sr (Figure 4c,d). Utilizing the Gatan Digital Micrograph technology, it is necessary to compute the interplanar *d*-spacing values of the samples. The *d*-spacing values for Fe_2O_3, St-Fe_2O_3, and various concentrations of Sr/St-Fe_2O_3 are 0.337, 0.297, 0.262, and 0.229 nm, respectively (Figure 4 a′−d′). These results for the interlayer *d*-spacing correspond very closely with the XRD data (JCPDS: 89-2810).

X-ray photoelectron spectroscopy (XPS) examination was recorded to look into how the dopant affected the chemical composition and electrical structure of the Fe_2O_3 NSs (Figure 5a,b). Spectra of O 1s after fitting are shown in Figure 5a. The oxygen linked to metal Fe (Fe−O) or lattice oxygen and the −OH surface hydroxyl species or deposited oxygen was responsible for the two primary peaks seen in the fitted O 1s spectra of samples, positioned at 529.4 and 531.1 eV.[53] Figure

https://doi.org/10.1021/acsomega.2c07980
ACS Omega 2023, 8, 8066−8077

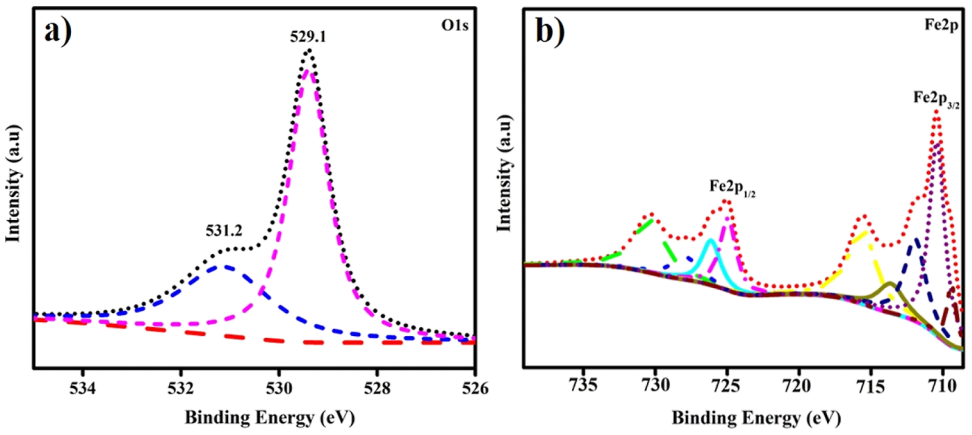

Figure 5. XPS spectra of Sr/St-Fe_2O_3 NSs: (a) O 1s and (b) Fe 2p.

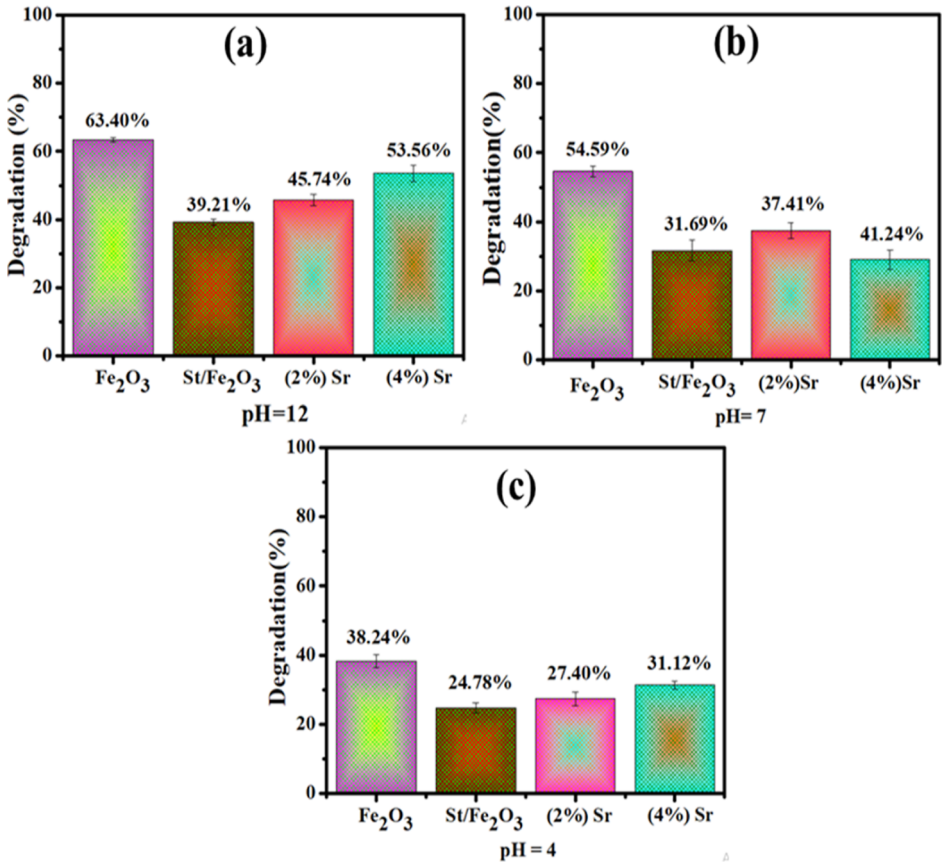

Figure 6. Photocatalysis for Fe_2O_3, St-Fe_2O_3, (2%) Sr/St-Fe_2O_3, and (4%) Sr/St-Fe_2O_3 in basic (a), neutral (b), and acidic media (c).

7b shows that the Fe $2p_{3/2}$ (711.3 eV) and Fe $2p_{1/2}$ (723.6 eV) peaks of Fe_2O_3 samples are closely matched with the published literature.[54−57] These peaks are positioned at 709.4−711.6 and 723.6−726.8 eV, respectively. For this reason, the presence of the binding energy (BE) peak at 712.6 eV, which was assigned to Fe^{3+} coupled with the −OH hydroxyl group, was taken as evidence for the occurrence of Fe^{3+} (Fe_2O_3).[55]

Surface elemental composition of fabricated Fe_2O_3, St-Fe_2O_3, and (2, 4%) Sr/St-Fe_2O_3 NSs is determined using energy-dispersive spectroscopic analysis, as shown in Figure S1a−d, respectively. The occurrence of composites of Fe_2O_3 was verified by the appearance of strong peaks of both Fe and O. The peak of carbon and Sr assured that St and Sr would be successfully incorporated into the structure of Fe_2O_3, as shown in Figure S1c,d. Consequently, the gold (Au) peak perceived in all concerned samples is ascribed to a coating composed of sputtered Au that covers the sample and helps the charge dissipate.[31,32] Additionally, a small quantity of Na was noticed, possibly due to the use of NaOH solution to keep pH levels stable throughout the synthesis process.[33,37]

The impact of pH on the PC degradation was evaluated by studying the PCA of pure and St-Fe_2O_3 and Sr/St-Fe_2O_3 NSs in the presence of Hg lamp light for the degradation of MB dye. From literature, the pH effects on PC properties are challenging to its multifaceted influence.[58] Adsorption plays a crucial role in the process because dye decomposition occurs on PC surfaces.[59] The performance of PCA is improved as pH rises because an excess of hydroxyl ions reacts with holes to

https://doi.org/10.1021/acsomega.2c07980
ACS Omega 2023, 8, 8066−8077

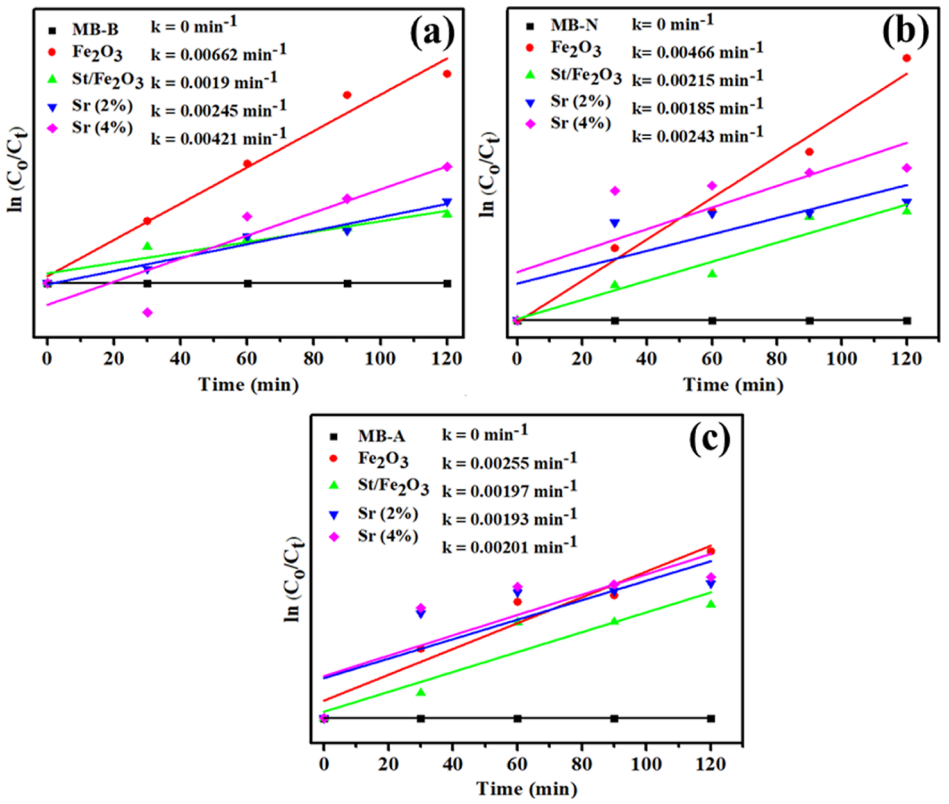

Figure 7. PCA for nanorods and plot of concentration of $\ln(C_0/C_t)$ vs time of Fe_2O_3, St-Fe_2O_3, (2%) Sr/St-Fe_2O_3, and (4%) Sr/St-Fe_2O_3 in basic (a), neutral (b), and acidic media (c).

create hydroxyl free radicals.[60] The performance of degradation is determined by adsorption with a radical hydroxyl concentration where a CB electron reacts with an oxygen molecule and converts it to an oxygen-free radical, and a hole in the VB reacts with a water molecule and splits it into a hydroxyl ion, and a hydrogen ion and hole react with hydroxyl ions to synthesize a hydroxyl-free radical.

The PCA of Fe_2O_3 NSs begins with photoexcitation of e^- from the VB to the CB, generating h^+ in the VB.

$$Fe_2O_3 + h\nu \text{ (photon)} \rightarrow h^+ \text{ (hole)} + e^- \text{(excited electron)}$$

The photogenerated e^- reacts with dissolved molecular oxygen (O_2) that adsorbed on the surface, forming superoxide radical anions ($^\bullet O_2^-$)

$$e^- + O_2 \rightarrow {}^\bullet O_2^-$$

These $^\bullet O_2^-$ radicals react with water molecules (H_2O) and generate oxidizing agents such as hydroperoxyl ($^\bullet HO_2$) and $^\bullet$OH radicals, acting as reactive agents to degrade organic pollutants.

$${}^\bullet O_2^- + H_2O \rightarrow {}^\bullet HO_2 + {}^\bullet OH$$

The photogenerated h^+ in the VB reacts with H_2O and hydroxide anions (OH^-) to form a highly reactive $^\bullet$OH radical.

$$h^+ + H_2O \rightarrow OH^- + H^+$$

$$h^+ + OH^- \rightarrow {}^\bullet OH$$

The hydroxyl- and oxygen-free radicals react with MB, converting MB into leucomethylene blue (LMB).[61] Two byproducts are obtained that are carbon dioxide and water and can be represented in Figure S2.

$$({}^\bullet O_2^-, {}^\bullet OH) + \text{Organic dye (MB)} \rightarrow CO_2 + H_2O$$

The degrading efficiency of the basic medium reduced from 63.4 to 53.5%, as represented in Figure 6a. An Fe_2O_3 catalyst was shown to have effective degrading performance in a basic medium with a maximum rate constant of 0.00662 min^{-1}. This may be explained by an increase in the amount of radical OH ions that have adsorbed on the surface of the catalyst, creating a negative net charge. Increased degradation efficiency after doping of Sr was the end product of the reaction between the anionic catalyst's surface and the cationic dye. Furthermore, at neutral pH (7), it can be seen that samples in a neutral medium degraded from 54.5 to 41.2% of MB in 120 min, as indicated in Figure 6b. The reduced PC performance may be due to a low electron−hole pair formation rate. At acidic pH (~4), we obtained 38.2 to 31.2% of MB degradation efficiency in 120 min, which is the minimum degradation of the as-prepared nanocatalyst compared to the efficiency mentioned above, as depicted in Figure 6c. A literature comparison of degradation with the current study can be represented in Table 1. By plotting linear curves of $\ln(C_t/C_0)$ against exposition time t, we obtained the pseudo-first-order kinetics-based value for k (the rate constant). This allowed us to calculate the rate constant represented in Figure 6a−c. It illustrates the kinetics of the degradation of specimens generated as a function of time with varying pH media.

The degree of mineralization was estimated by measuring total organic carbon (TOC) in treated water. The investigation was conducted on St-Fe_2O_3 and Sr/St-Fe_2O_3 (2 and 4%) at various time intervals up to 180 min. This investigation (Figure

https://doi.org/10.1021/acsomega.2c07980
ACS Omega 2023, 8, 8066−8077

Table 1. Literature Comparison of Degradation with the Current Study

samples	dye	degradation performance (%)	reference
Fe_2O_3	MB	57	62
Fe_3O_4	MB	85.33	63
Mo−Fe_3O_4	MB	86.25	63
Cu−Fe_2O_3	MB	58.57	64
Fe_2O_3	MB	63	present work

8) indicated that the TOC of produced compounds under visible light irradiation decreased steadily with reaction time,

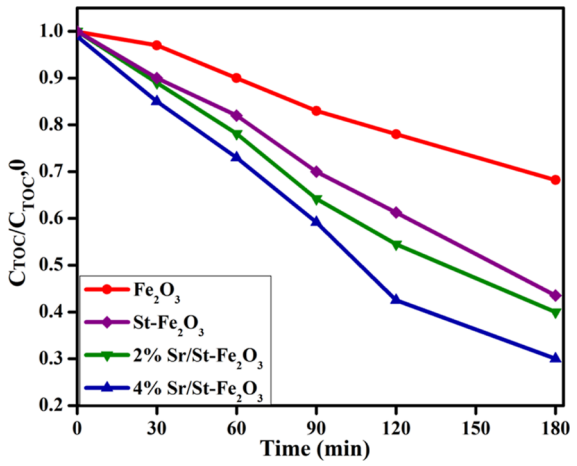

Figure 8. Variation of TOC for synthesized NSs.

and a considerable quantity of mineralization of dye was noticed after 180 min in Sr/St-Fe_2O_3 (4%). Moreover, results suggest that the dye may undergo a series of intermediate transformations before its deterioration ultimately leads to its complete mineralization.[65,66]

The bactericidal effectiveness of bare Fe_2O_3, St/Fe_2O_3, and (2, 4 wt %) Sr/St-doped Fe_2O_3 NSs was obtained from inhibition zone measurements via an agar-well diffusion assay for *S. aureus* (G +ve) and *E. coli* (G −ve) as mentioned in Table 2. Specific concentrations (1.0 mg/50 μL and 0.5 mg/50 μL) of bare and Sr/St-Fe_2O_3 NSs were filled in concerning wells, and CF (0.05 mg/50 μL) was utilized as a positive control for the comparison; meanwhile, DI water (50 μL) was used as the negative control.[37,49] Results showed a significant association between the inhibition zones and NS concentration. Significant inhibition zones ($P < 0.05$) were captured for each of the samples listed in ranges of 0−0.47 mm and 0−2.40 mm for lower and higher concentrations against *S. aureus* and subsequently 0−3.55 mm and 1.05−4.60 mm against *E. coli*, respectively. The results showed improved effectiveness (P 0.05) against both bacteria. CF has an inhibition zone toward *S. aureus* (9.20 mm) and for *E. coli* (5.35 mm) as opposed to DI water (0 mm). 4% Sr/St-Fe_2O_3 revealed promising bactericidal effectiveness against G +ve relative to G −ve at lower and higher concentrations, primarily due to changes in the bacterial membrane structure. Reactive oxygen species (ROS) generation can be represented in reaction mechanism eqs 2−7

$$Fe_2O_3 + h\nu\ (\text{photon}) \rightarrow h^+\ (\text{hole}) + e^-\ (\text{excited electron}) \quad (2)$$

$$e^- + O_2 \rightarrow {}^*O_2^- \quad (3)$$

$$h^+ + H_2O \rightarrow OH^- + H^+ \quad (4)$$

$${}^*O_2^- + H^+ \rightarrow {}^*HO_2 \quad (5)$$

$${}^*HO_2 + e^- + H^+ \rightarrow {}^*H_2O_2 \quad (6)$$

$${}^*H_2O_2 + {}^*O_2^- \rightarrow {}^*OH + O_2 + OH^- \quad (7)$$

Pure and Sr/St−St co-doped Fe_2O_3 are exposed to light with the energy of the photon equal to the energy band gap of the semiconductor, and electrons from the VB are transferred to the CB, leaving holes in the VB. These excited electrons (e^-) in the CB can be trapped by the oxygen molecules (O_2) present on the surface, producing superoxide anion radicals. Similarly, the holes in the VB react with the water molecules (H_2O), emitting hydroxyl and hydrogen ions. The superoxide anion radicals (O^{2-}) interact with H^+ ions to produce the hydroperoxyl radical ($^*HO_2$). The hydroperoxyl radical ($^*HO_2$) combines with e^- and H^+, resulting in the hydrogen peroxide radical ($^*H_2O_2$). The mechanism reaction of antimicrobial activity can be represented in the reaction,[67] where ROS play an influential role in the death of infectious bacteria, as represented in Figure S3. The direct attack of the prepared material damages the cell wall and cell membrane of bacteria owing to the microorganism death. The antimicrobial activity is divulged when NSs produce intracellular ROS and communicate with the nucleic acid of a bacterial cell that promotes single- and dual-wrecked breaks within the nitrogenous base and sugar−phosphate bond of nucleic acid.[68] This is accomplished by promoting the oxidation of leftover amino acids and unplugging essential proteins, disrupting various metabolic activities.[69,70] As a result, ROS may harm nucleic acid, and ROS is likely to blame for DNA breaks in bacterial cells, ultimately leading to the death of bacteria.[37] Lysis and the collapse of bacterial cells result from an interaction between such a strong electrostatic charge (Fe^{3+}) and a bacterial

Table 2. Antimicrobial Activity of Fe_2O_3, St/Fe_2O_3, and (2, 4%) Sr with Different Concentrations

	S. aureus		*E. coli*	
	inhibition zone (mm)		inhibition zone (mm)	
samples	0.5 mg/50 μL	1.0 mg/50 μL	0.5 mg/50 μL	1.0 mg/50 μL
Fe_2O_3				1.05
St-Fe2O3			2.10	3.15
2% Sr/St-Fe_2O_3		1.30	2.75	4.05
4% Sr/St-Fe2O3	0.47	2.40	3.55	4.60
CF	9.20	9.20	5.35	5.35
DIW	0	0	0	0

https://doi.org/10.1021/acsomega.2c07980
ACS Omega 2023, 8, 8066−8077

membrane. This interaction ultimately ends in the death of the bacteria that were involved. When there is a higher concentration of the NSs, there is also an increase in their potential to kill bacteria.[69]

Interest in molecular docking predictions has increased dramatically over the last several decades due to its potential as a powerful method for studying a wide range of biological processes. It has been well documented[71−73] that DHFR (i.e., folate production) is crucial to discovering new antibiotics. Although the antimicrobial activity of several NSs has been apparent in recent years, further research into the mechanisms behind these activities is required.[74,75] The best-docked conformation of the DHFR enzyme against *E. coli* for St-Fe_2O_3 showed H-bonding interactions with Ile-5, Ala-6, Ala-7, Asn-18, Ser-49, Ile-94, Gly-97, and Thr-146, leading to a binding score of 6.70 as represented in Figure S4a,b. In contrast, the best-docked conformation for Sr/St-Fe_2O_3 showed metal contact interaction with Ala-7, Tyr-100, Ile-94, and Leu-28 with an overall binding score of 7.76 as depicted in Figure S4c.

St/Fe_2O_3 NSs binding to the active pocket of the DHFR *S. aureus* enzyme exhibited a similar pattern, with an overall binding energy of 4.13. Figure S5c shows that the H-bond interactions with Asn-18, Ser-49, Ala-7, Ile-14, and Gly-93 were especially prominent. The molecular docking predictions of Sr/St-Fe_2O_3 NSs against *S. aureus* indicated H-bonds with critical amino acid residues, including Asp-27, Ala-7, Phe-92, and Trp-22, with a total binding score of 5.79 as shown in Figure S5b. Molecular docking predictions agreed with in vitro bactericidal activities against *E. coli*, indicating that inhibition of the DHFR enzyme may be a mechanism controlling the antibacterial activity of new Sr/St-Fe_2O_3 NSs (Figure S5c).

4. CONCLUSIONS

In this study, the successful synthesis of pristine Fe_2O_3, St/Fe_2O_3, and Sr with different concentration (2, 4 wt %) was carried out using the co-precipitation route to evaluate PCA using MB dye, and bactericidal activities against *S. aureus* and *E. coli* bacteria and silico docking studies against DHFR enzyme were also carried out. XRD analysis verified the rhombohedral crystal structure, and the calculated crystalline size was measured as 48.41, 42.83, 39.51, and 35.72 nm for pure and doped samples, respectively, using intense peaks (012), (104), and (110), respectively, by applying the Debye−Scherrer formula. The SAED pattern also confirms the polycrystalline nature of the synthesized sample. FTIR analysis confirms the presence of the Fe−O functional group. Plane orientation and *d*-spacing have been affirmed by XRD that agreed with the HR-TEM findings. UV−vis divulged an E_g of 2.78 eV for peak ∼435 nm and displayed a blue shift that might be attributable to the doping action of St and Sr. PL spectra indicated the electron−hole recombination rate that decreases the PCA. Compared with co-doped Fe_2O_3, pristine samples degraded MB up to 63.40, 54.59, and 38.24% in basic, neutral, and acidic media, respectively. The synthesized NSs displayed high bactericidal effectiveness against *S. aureus* and *E. coli* germs. The synthesized nanocatalyst showed remarkable antibacterial action against *E. coli* bacteria rather than *S. aureus* at high and low doses compared to CF. In silico studies showed good agreement with in vitro bactericidal activities against *E. coli* against the DHFR enzyme for Sr/St-Fe_2O_3 showing H-bonding interactions with Ala-7, Tyr-100, Ile-94, and Leu-28.

■ ASSOCIATED CONTENT

Data Availability Statement

All Research Data is found in this manuscript.

Supporting Information

The Supporting Information is available free of charge at https://pubs.acs.org/doi/10.1021/acsomega.2c07980.

EDS analysis for Fe_2O_3, St/Fe_2O_3, and Sr/St co-doped Fe_2O_3 with the Sr content (2, 4 wt %); schematic diagram for PC degradation of MB dye; antibacterial mechanism of produced Fe_3O_4 and Sr/St-doped Fe_3O_4 described schematically; binding pocket and binding interaction pattern with active site residues of the DHFR enzyme from *E. coli*, St-Fe_2O_3, and Sr/St-Fe_2O_3; binding pocket of DHFR from *S. aureus;* and binding interaction pattern with active site residues of enzyme DHFR, Sr/St-Fe_2O_3, and St-Fe_2O_3 (PDF)

■ AUTHOR INFORMATION

Corresponding Authors

Muhammad Ikram − *Solar Cell Applications Research Lab, Department of Physics, Government College University Lahore, Lahore 54000, Pakistan;* orcid.org/0000-0001-7741-789X; Email: dr.muhammadikram@gcu.edu.pk

Walid Nabgan − *Departament d'Enginyeria Química, Universitat Rovira i Virgili, Tarragona 43007, Spain;* Email: walid.nabgan@urv.cat

Ali Al-Shanini − *College of Petroleum and Engineering, Hadhramout University, Mukalla, Hadhramout 50512, Yemen;* orcid.org/0000-0002-7616-7814; Email: a.alshanini@hu.edu.ye

Authors

Anum Shahzadi − *Faculty of Pharmacy, The University of Lahore, Lahore 54000, Pakistan*

Ali Haider − *Department of Clinical Sciences, Faculty of Veterinary and Animal Sciences, Muhammad Nawaz Shareef University of Agriculture, Multan 66000, Pakistan*

Muhammad Imran − *Department of Chemistry, Government College University Faisalabad, Sahiwal, Punjab 57000, Pakistan*

Shaukat Hayat − *Department of Physics, Riphah Institute of Computing and Applied Sciences (RICAS), Riphah International University, Lahore 54000, Pakistan*

Junaid Haider − *Tianjin Institute of Industrial Biotechnology, Chinese Academy of Sciences, Tianjin 300308, China;* orcid.org/0000-0002-2254-1196

Anwar Ul-Hamid − *Core Research Facilities, King Fahd University of Petroleum & Minerals, Dhahran 31261, Saudi Arabia;* orcid.org/0000-0002-0259-301X

Faiz Rasool − *Department of Physics, Riphah Institute of Computing and Applied Sciences (RICAS), Riphah International University, Lahore 54000, Pakistan*

Muhammad Mustajab − *Solar Cell Applications Research Lab, Department of Physics, Government College University Lahore, Lahore 54000, Pakistan*

Salamat Ali − *Department of Physics, Riphah Institute of Computing and Applied Sciences (RICAS), Riphah International University, Lahore 54000, Pakistan*

Complete contact information is available at: https://pubs.acs.org/10.1021/acsomega.2c07980

https://doi.org/10.1021/acsomega.2c07980
ACS Omega 2023, 8, 8066−8077

Funding

This research was funded by the higher education commission (HEC) of Pakistan

Notes

The authors declare no competing financial interest.

■ ACKNOWLEDGMENTS

Authors are thankful to HEC, Pakistan, via Project NRPU-20-17615 (M.I.).

■ REFERENCES

(1) Naseem, T.; Durrani, T. The role of some important metal oxide nanoparticles for wastewater and antibacterial applications: A review. *Environ. Chem. Ecotoxicol.* **2021**, *3*, 59−75.
(2) Chowdhury, R.; Khan, A.; Rashid, M. H. Green synthesis of CuO nanoparticles using: Lantana camara flower extract and their potential catalytic activity towards the aza-Michael reaction. *RSC Adv.* **2020**, *10*, 14374−14385.
(3) Sarma, G. K.; Khan, A.; El-Toni, A. M.; Rashid, M. H. Shape-tunable CuO-Nd(OH)3 nanocomposites with excellent adsorption capacity in organic dye removal and regeneration of spent adsorbent to reduce secondary waste. *J. Hazard. Mater.* **2019**, *380*, 120838.
(4) Salem, I. A. Kinetics and mechanism of the color removal from congo red with hydrogen peroxide catalyzed by supported zirconium oxide. *Transition Met. Chem.* **2000**, *25*, 599−604.
(5) Siddiqui, S. I.; Manzoor, O.; Mohsin, M.; Chaudhry, S. A. Nigella sativa seed based nanocomposite-MnO2/BC: An antibacterial material for photocatalytic degradation, and adsorptive removal of Methylene blue from water. *Environ. Res.* **2019**, *171*, 328−340.
(6) Lu, W.; Li, J.; Sheng, Y.; Zhang, X.; You, J.; Chen, L. One-pot synthesis of magnetic iron oxide nanoparticle-multiwalled carbon nanotube composites for enhanced removal of Cr(VI) from aqueous solution. *J. Colloid Interface Sci.* **2017**, *505*, 1134−1146.
(7) Rodriguez-Narvaez, O. M.; et al. Treatment Technologies for Emerging Contaminants in water: A review. *Chem. Eng.* **2017**, *22*, 361.
(8) Zhu, S.; Wang, D. Photocatalysis: Basic principles, diverse forms of implementations and emerging scientific opportunities. *Adv. Energy Mater.* **2017**, *7*, 1700841.
(9) Zhao, L.; Deng, J.; Sun, P.; Liu, J.; Ji, Y.; Nakada, N.; Qiao, Z.; Tanaka, H.; Yang, Y. Nanomaterials for treating emerging contaminants in water by adsorption and photocatalysis: Systematic review and bibliometric analysis. *Sci. Total Environ.* **2018**, *627*, 1253−1263.
(10) Tara, N.; Siddiqui, S. I.; Bach, Q. V.; Chaudhry, S. A. Reduce graphene oxide-manganese oxide-black cumin based hybrid composite (rGO-MnO2/BC): A novel material for water remediation. *Mater. Today Commun.* **2020**, *25*, 101560.
(11) Salata, O. V. Applications of nanoparticles in biology and medicine. *J. Nanobiotechnol.* **2004**, *2*, 123−128.
(12) Huber, D. L. Synthesis, properties, and applications of iron nanoparticles. *Small* **2005**, *1*, 482−501.
(13) Burstein, G. T. The iron oxides: Structure, properties, reactions, occurrence and uses. *Corros. Sci.* **1997**, *39*, 1499−1500.
(14) Mou, X.; Zhang, B.; Li, Y.; Yao, L.; Wei, X.; Su, D. S.; Shen, W. Rod-shaped Fe_2O_3 as an efficient catalyst for the selective reduction of nitrogen oxide by ammonia. *Angew. Chem., Int. Ed.* **2012**, *51*, 2989−2993.
(15) Guo, S.; Zhang, G.; Guo, Y.; Yu, J. C. Graphene oxide-Fe2O3 hybrid material as highly efficient heterogeneous catalyst for degradation of organic contaminants. *Carbon* **2013**, *60*, 437−444.
(16) Basińska, A.; Jóźwiak, W. K.; Góralski, J.; Domka, F. The behaviour of Ru/Fe2O3 catalysts and Fe2O3 supports in the TPR and TPO conditions. *Appl. Catal., A* **2000**, *190*, 107−115.
(17) Liu, H.; Kozlov, A. I.; Kozlova, A. P.; Shido, T.; Asakura, K.; Iwasawa, Y. Active oxygen species and mechanism for low-temperature CO oxidation reaction on a TiO2-supported Au catalyst prepared from Au(PPh3)(NO3) and as-precipitated titanium hydroxide. *J. Catal.* **1999**, *185*, 252−264.
(18) Wang, G. H.; Li, W. C.; Jia, K. M.; Spliethoff, B.; Schüth, F.; Lu, A. H. Shape and size controlled α-Fe2O3 nanoparticles as supports for gold-catalysts: Synthesis and influence of support shape and size on catalytic performance. *Appl. Catal., A* **2009**, *364*, 42−47.
(19) Yan, W.; Jianliang, C.; Shurong, W.; Xianzhi, G.; Jun, Z.; Huijuan, X.; Shoumin, Z.; Shihua, W. Facile synthesis of porous α-Fe2O3 nanorods and their application in ethanol sensors. *J. Phys. Chem. C* **2008**, *112*, 17804−17808.
(20) Chen, J.; Xu, L.; Li, W.; Gou, X. α-Fe2O3 nanotubes in gas sensor and lithium-ion battery applications. *Adv. Mater.* **2005**, *17*, 582−586.
(21) Mahdavian, A. R.; Mirrahimi, M. A. S. Efficient separation of heavy metal cations by anchoring polyacrylic acid on superparamagnetic magnetite nanoparticles through surface modification. *Chem. Eng. J.* **2010**, *159*, 264−271.
(22) Xu, P.; Zeng, G. M.; Huang, D. L.; Feng, C. L.; Hu, S.; Zhao, M. H.; Lai, C.; Wei, Z.; Huang, C.; Xie, G. X.; Liu, Z. F. Use of iron oxide nanomaterials in wastewater treatment: A review. *Sci. Total Environ.* **2012**, *424*, 1−10.
(23) Bel Haaj, S.; Magnin, A.; Pétrier, C.; Boufi, S. Starch nanoparticles formation via high power ultrasonication. *Carbohydr. Polym.* **2013**, *92*, 1625−1632.
(24) Zhu, F. Structures, properties, modifications, and uses of oat starch. *Food Chem.* **2017**, *229*, 329−340.
(25) Pal, S.; Mal, D.; Singh, R. P. Cationic starch: An effective flocculating agent. *Carbohydr. Polym.* **2005**, *59*, 417−423.
(26) Kenawy, E. R.; Kamoun, E. A.; Mohy Eldin, M. S.; El-Meligy, M. A. Physically crosslinked poly(vinyl alcohol)-hydroxyethyl starch blend hydrogel membranes: Synthesis and characterization for biomedical applications. *Arabian J. Chem.* **2014**, *7*, 372−380.
(27) Mukherjee, S.; Mishra, M. Application of strontium-based nanoparticles in medicine and environmental sciences. *Nanotechnol. Environ. Eng.* **2021**, *6*, 25.
(28) Mustajab, M.; Ikram, M.; Ali, H.; Ul-Hamid, A.; Nabgan, W.; Haider, J.; Ghaffar, R.; Shahzadi, A.; Abdul, G.; Saeed, A. Promising performance of polyvinylpyrrolidone-doped bismuth oxyiodide quantum dots for antibacterial and catalytic applications. *Appl. Nanosci.* **2022**, *12*, 2621−2633.
(29) Wu, Z. G.; Gao, J. F. Synthesis of γ-Fe 2O 3 nanoparticles by homogeneous co-precipitation method. *Micro Nano Lett.* **2012**, *7*, 533−535.
(30) Ikram, M.; Hayat, S.; Imran, M.; Haider, A.; Naz, S.; Ul-Hamid, A.; Shahzadi, I.; Haider, J.; Shahzadi, A.; Nabgan, W.; Ali, S. Novel Ag/cellulose-doped CeO2 quantum dots for efficient dye degradation and bactericidal activity with molecular docking study. *Carbohydr. Polym.* **2021**, *269*, 118346.
(31) Ikram, M.; Inayat, T.; Haider, A.; Ul-Hamid, A.; Haider, J.; Nabgan, W.; Saeed, A.; Shahbaz, A.; Hayat, S.; Ul-Ain, K.; Butt, A. R. Graphene Oxide-Doped MgO Nanostructures for Highly Efficient Dye Degradation and Bactericidal Action. *Nanoscale Res. Lett.* **2021**, *16*, 56.
(32) Ikram, M.; Imran, M.; Hayat, S.; Shahzadi, A.; Haider, A.; Naz, S.; Ul-Hamid, A.; Nabgan, W.; Fazal, I.; Ali, S. MoS2/cellulose-doped ZnO nanorods for catalytic, antibacterial and molecular docking studies. *Nanoscale Adv.* **2022**, *4*, 211−225.
(33) Ikram, M.; Shahzadi, A.; Hayat, S.; Nabgan, W.; Ul-Hamid, A.; Haider, A.; Noor, M.; Goumri-Said, S.; Kanoun, M. B.; Ali, S. Novel Ta/chitosan-doped CuO nanorods for catalytic purification of industrial wastewater and antimicrobial applications. *RSC Adv.* **2022**, *12*, 16991−17004.
(34) Hawser, S.; Lociuro, S.; Islam, K. Dihydrofolate reductase inhibitors as antibacterial agents. *Biochem. Pharmacol.* **2006**, *71*, 941−948.
(35) Summerfield, R. L.; Daigle, D. M.; Mayer, S.; Mallik, D.; Hughes, D. W.; Jackson, S. G.; Sulek, M.; Organ, M. G.; Brown, E. D.; Junop, M. S. A 2.13 Å structure of E. coli dihydrofolate reductase bound to a novel competitive inhibitor reveals a new binding surface involving the M20 loop region. *J. Med. Chem.* **2006**, *49*, 6977−6986.

https://doi.org/10.1021/acsomega.2c07980
ACS Omega 2023, 8, 8066−8077

(36) Oefner, C.; Parisi, S.; Schulz, H.; Lociuro, S.; Dale, G. E. Inhibitory properties and X-ray crystallographic study of the binding of AR-101, AR-102 and iclaprim in ternary complexes with NADPH and dihydrofolate reductase from Staphylococcus aureus. *Acta Crystallogr., Sect. D: Biol. Crystallogr.* **2009**, *65*, 751−757.
(37) Mehmood, Z.; Ikram, M.; Imran, M.; Shahzadi, A.; Haider, A.; Ul-Hamid, A.; Nabgan, W.; Haider, J.; Hayat, S. Z. officinale-doped silver/calcium oxide nanocomposites: Catalytic activity and antimicrobial potential with molecular docking analysis. *Process Biochem.* **2022**, *121*, 635−646.
(38) Radhakrishnan, S.; Krishnamoorthy, K.; Sekar, C.; Wilson, J.; Kim, S. J. A highly sensitive electrochemical sensor for nitrite detection based on Fe2O3 nanoparticles decorated reduced graphene oxide nanosheets. *Appl. Catal., B* **2014**, *148−149*, 22−28.
(39) Kumar, K. V. A.; Chandana, L.; Ghosal, P.; Subrahmanyam, C. Simultaneous photocatalytic degradation of p-cresol and Cr (VI) by metal oxides supported reduced graphene oxide. *Mol. Catal.* **2018**, *451*, 87−95.
(40) Fard, G. C.; Mirjalili, M.; Najafi, F. Preparation of nanocellulose/A-Fe2O3 hybrid nanofiber for the cationic dyes removal: Optimization characterization, kinetic, isotherm and error analysis. *Bulg. Chem. Commun.* **2018**, *50*, 251−261.
(41) Sobhanardakani, S.; Jafari, A.; Zandipak, R.; Meidanchi, A. Removal of heavy metal (Hg(II) and Cr(VI)) ions from aqueous solutions using Fe2O3@SiO2 thin films as a novel adsorbent. *Process Saf. Environ. Prot.* **2018**, *120*, 348−357.
(42) Zhang, N.; Zheng, J. Synthesis of Ag−Fe2O3−RGO nanocomposites for the electrocatalytic reduction of H2O2. *J. Mater. Sci.: Mater. Electron.* **2017**, *28*, 11209−11216.
(43) Qin, W.; Yang, C.; Yi, R.; Gao, G. Hydrothermal synthesis and characterization of single-crystalline α-Fe2O3 nanocubes. *J. Nanomater.* **2011**, *2011*, 159259.
(44) Schwaminger, S. P.; Surya, R.; Filser, S.; Wimmer, A.; Weigl, F.; Fraga-García, P.; Berensmeier, S. Formation of iron oxide nanoparticles for the photooxidation of water: Alteration of finite size effects from ferrihydrite to hematite. *Sci. Rep.* **2017**, *7*, 12609.
(45) Archana, V.; Joseph Prince, J.; Kalainathan, S. Simple One-Step Leaf Extract-Assisted Preparation of α -Fe2O3Nanoparticles, Physicochemical Properties, and Its Sunlight-Driven Photocatalytic Activity on Methylene Blue Dye Degradation. *J. Nanomater.* **2021**, *2021*, 8570351.
(46) Mizuno, S.; Yao, H. On the electronic transitions of α-Fe2O3 hematite nanoparticles with different size and morphology: Analysis by simultaneous deconvolution of UV−vis absorption and MCD spectra. *J. Magn. Magn. Mater.* **2021**, *517*, 167389.
(47) Faridi, A. W.; Imran, M.; Tariq, G. H.; Ullah, S.; Noor, S. F.; Ansar, S.; Sher, F. "Synthesis and Characterization of High-Efficiency Halide Perovskite Nanomaterials for Light-Absorbing Applications". *Ind. Eng. Chem. Res.*, **2022**, DOI: 10.1021/acs.iecr.2c00416.
(48) Ikram, M.; Abid, N.; Haider, A.; Ul-Hamid, A.; Haider, J.; Shahzadi, A.; Nabgan, W.; Goumri-Said, S.; Butt, A. R.; Benali Kanoun, M. Toward efficient dye degradation and the bactericidal behavior of Mo-doped La2O3nanostructures. *Nanoscale Adv.* **2022**, *4*, 926−942.
(49) Khan, A. D.; Ikram, M.; Haider, A.; Ul-Hamid, A.; Nabgan, W.; Haider, J. Polyvinylpyrrolidone and chitosan-doped lanthanum oxide nanostructures used as antibacterial agents and nanocatalyst. *Appl. Nanosci.* **2022**, *12*, 2227−2239.
(50) Mafa, P. J.; Mamba, B. B.; Kuvarega, A. T. Construction of hierarchical BiPW12O40/BiOI p−n heterojunction with enhanced visible light activity for degradation of endocrine disrupting Bisphenol A. *Sep. Purif. Technol.* **2020**, *253*, 117349.
(51) Manikandan, A.; Saravanan, A.; Antony, S.; Bououdina, M. One-pot low temperature synthesis and characterization studies of nanocrystalline α-Fe2O3 based dye sensitized solar cells. *J. Nanosci. Nanotechnol.* **2015**, *15*, 4358−4366.
(52) Lassoued, A.; Lassoued, M. S.; Dkhil, B.; Ammar, S.; Gadri, A. Synthesis, photoluminescence and Magnetic properties of iron oxide (α-Fe2O3) nanoparticles through precipitation or hydrothermal methods. *Phys. E* **2018**, *101*, 212−219.
(53) Min, F.; Yang, S.; Zhang, Q.; Yang, C.; Gao, W.; Wang, S.; Teng, F.; Li, G.; Ai, Z. Cu-Doped α-Fe2O3 Microspheres as Anode Materials for Lithium-Ion Batteries. *J. Nanosci. Nanotechnol.* **2018**, *18*, 4296.
(54) Shikha, P.; Randhawa, B.; Kang, T. Greener synthetic route for superparamagnetic and luminescent α-Fe_2O_3 nanoparticles in binary mixtures of ionic liquid and ethylene glycol. *RSC Adv.* **2015**, *5*, 51158.
(55) Tahir, A. A.; Wijayantha, K. G.; Saremi-Yarahmadi, S.; Mazhar, M.; McKee, V. Nanostructured α-Fe2O3 Thin Films for Photoelectrochemical Hydrogen Generation. *Chem. Mater.* **2009**, *21*, 3763.
(56) Ding, J.; Zhong, Q. Simultaneous removal of NO X and SO 2 with H 2 O 2 over Fe based catalysts at low temperature. *RSC Adv.* **2014**, *4*, 5394.
(57) Tang, R.; Jiang, C.; Qian, W.; Jian, J.; Zhang, X.; Wang, H.; Yang, H. Dielectric relaxation, resonance and scaling behaviors in Sr3Co2Fe24O41 hexaferrite. *Sci. Rep.* **2015**, *5*, 13645.
(58) Young, K.; Jayasuriya, H.; Ondeyka, J. G.; Herath, K.; Zhang, C.; Kodali, S.; Galgoci, A.; Painter, R.; Brown-Driver, V.; Yamamoto, R.; Silver, L. L.; Zheng, Y.; Ventura, J. I.; Sigmund, J.; Ha, S.; Basilio, A.; Vicente, F.; Tormo, J. R.; Pelaez, F.; Youngman, P.; Cully, D.; Barrett, J. F.; Schmatz, D.; Singh, S. B.; Wang, J. Discovery of FabH/FabF inhibitors from natural products. *Antimicrob. Agents Chemother.* **2006**, *50*, 519−526.
(59) Kadam, A. N.; Kim, T. G.; Shin, D. S.; Garadkar, K. M.; Park, J. Morphological evolution of Cu doped ZnO for enhancement of photocatalytic activity. *J. Alloys Compd.* **2017**, *710*, 102−113.
(60) Lu, C.; Wu, Y.; Mai, F.; Chung, W.; Wu, C.; Lin, W.; Chen, C. Degradation efficiencies and mechanisms of the ZnO-mediated photocatalytic degradation of Basic Blue 11 under visible light irradiation. *J. Mol. Catal. A: Chem.* **2009**, *310*, 159−165.
(61) Jamal, F.; Ikram, M.; Ali, H.; Ul-Hamid, A.; Ijaz, M.; Nabgan, W.; Haider, J.; Shahzadi, I. Facile synthesis of silver and polyacrylic acid doped magnesium oxide nanostructure for photocatalytic dye degradation and bactericidal behavior. *Appl. Nanosci.* **2022**, *12*, 2409.
(62) Teo, P.-S.; Pandikumar, A.; Ngee, L. H.; Ming, H. N.; Hua, C. C. Magnetically separable reduced graphene oxide/iron oxide nanocomposite materials for environmental remediation. *Catal. Sci. Technol.* **2014**, *4*, 4396−4405.
(63) Shujah, T.; Shahzadi, A.; Ali, H.; Mustajab, M.; Haider, A. M.; Ul-Hamid, A.; Haider, J.; Nabgan, W.; Ikram, M. Molybdenum-doped iron oxide nanostructures synthesized via a chemical co-precipitation route for efficient dye degradation and antimicrobial performance: in silico molecular docking studies. *RSC Adv.* **2022**, *12*, 35177−35191.
(64) Haider, S.; Saad Shar, S.; Shakir, I.; Philips, O.; Agboola. Visible light active Cu-doped iron oxide for photocatalytic treatment of methylene blue. *Ceram. Int.* **2022**, *48*, 7605−7612.
(65) Ikram, M.; Jamal, F.; Haider, A.; Dilpazir, S.; Shujah, T.; Naz, M.; Imran, M.; Ul-Hamid, A.; Shahzadi, I.; Ullah, H.; Nabgan, W. Efficient Photocatalytic Dye Degradation and Bacterial Inactivation by Graphitic Carbon Nitride and Starch-Doped Magnesium Hydroxide Nanostructures. *ACS Omega* **2022**, *7*, 39998−40008.
(66) Bilal, M.; Ikram, M.; Shujah, T.; Haider, A.; Naz, S.; Ul-Hamid, A.; Naz, M.; Haider, J.; Shahzadi, I.; Nabgan, W. Chitosan-Grafted Polyacrylic Acid-Doped Copper Oxide Nanoflakes Used as a Potential Dye Degrader and Antibacterial Agent: In Silico Molecular Docking Analysis. *ACS Omega* **2022**, *7*, 41614−41626.
(67) Ikram, M.; Haider, H.; Imran, M.; Haider, J.; Naz, S.; Ul-Hamid, A.; Nabgan, W.; Mustajab, M.; Shahzadi, A.; Shahzadi, I.; Raza, M.; Nazir, G. Facile synthesis of starch and tellurium doped SrO nanocomposite for catalytic and antibacterial potential: In silico molecular docking studies. *Int. J. Biol. Macromol.* **2022**, *221*, 496−507.
(68) Ragab, E.; Shaban, M.; Khalek, A. A.; Mohamed, F. Design and characterization of PANI/starch/Fe2O3 bio composite for wastewater remediation. *Int. J. Biol. Macromol.* **2021**, *181*, 301−312.
(69) Aziz, W. J.; Abid, M. A.; Kadhim, D. A.; Mejbel, M. K. Synthesis of iron oxide (β-fe2o3) nanoparticles from Iraqi grapes

extract and its biomedical application. *IOP Conf. Ser.: Mater. Sci. Eng.* **2020**, *881*, 012099.
(70) Dash, P.; Raut, S.; Jena, M.; Nayak, B. Harnessing the biomedical properties of ferromagnetic α-Fe2O3 NPs with a plausible formation mechanism. *Ceram. Int.* **2020**, *46*, 26190−26204.
(71) Mullis, M. M.; Rambo, I. M.; Baker, B. J.; Reese, B. K. Diversity, Ecology, and Prevalence of Antimicrobials in Nature. *Front. Microbiol.* **2019**, *10*, 2518.
(72) Higgins, D. L.; Chang, R.; Debabov, D. V.; Leung, J.; Wu, T.; Krause, K. M.; Sandvik, E.; Hubbard, J. M.; Kaniga, K.; Schmidt, D. E.; Gao, Q.; Cass, R. T.; Karr, D. E.; Benton, B. M.; Humphrey, P. P. Telavancin, a multifunctional lipoglycopeptide, disrupts both cell wall synthesis and cell membrane integrity in methicillin-resistant Staphylococcus aureus. *Antimicrob. Agents Chemother.* **2005**, *49*, 1127−1134.
(73) Shaikh, S.; Fatima, J.; Shakil, S.; Rizvi, S. M. D.; Kamal, M. A. Antibiotic resistance and extended spectrum beta-lactamases: Types, epidemiology and treatment. *Saudi J. Biol. Sci.* **2015**, *22*, 90.
(74) Bury, N. R.; Wood, C. M. Mechanism of branchial apical silver uptake by rainbow trout is via the proton-coupled Na+ channel. *Am. J. Physiol.* **1999**, *277*, R1385.
(75) Arsalan, A.; Younus, H. Enzymes and nanoparticles: Modulation of enzymatic activity via nanoparticles. *Int. J. Biol. Macromol.* **2018**, *118*, 1833−1847.

https://doi.org/10.1021/acsomega.2c07980
ACS Omega 2023, 8, 8066−8077